Unveiling the origin of a nonequilibrium dynamic process detected by X-ray photon correlation spectroscopy *via* a finite element analysis approach

Li Ma,[a] Fan Zhang,[b]* Andrew Allen[b] and Lyle Levine[a]

[a]Materials Science and Engineering Division, National Institute of Standards and Technology, 100 Bureau Drive, Gaithersburg, MD 20899, USA, and [b]Materials Measurement Science Division, National Institute of Standards and Technology, 100 Bureau Drive, Gaithersburg, MD 20899, USA. Correspondence e-mail: fan.zhang@nist.gov

It is a scientific and engineering challenge to characterize materials under nonequilibrium conditions. In recent years, X-ray photon correlation spectroscopy (XPCS), a synchrotron-based coherent X-ray scattering technique, has been found useful in determining the timescales associated with various nonequilibrium processes, with detailed descriptions of the underlying processes lacking. Here, both static ultra small angle X-ray scattering (USAXS) and dynamic USAXS-based XPCS were used to investigate a transient structural change (a nonequilibrium process) associated with an isothermal anneal in a glass polymer composite system. While the bulk USAXS technique lacked the required sensitivity to detect the change in the microstructures, the local structural reorganization was apparent in the XPCS study. The structural changes were modeled using a three-dimensional finite element analysis approach and wave-propagation theory was used to simulate the resulting reciprocal-space coherent scattering intensity. Qualitative agreement was found between the modeling and experimental results, which validates that stress relaxation in the viscous polymer matrix was responsible for the observed changes. This analysis demonstrates that multi-physics modeling of complex systems can be used to interpret XPCS measurements of nonequilibrium processes.

1. Introduction

Characterization of material dynamics in equilibrium, and in particular, nonequilibrium, is a well documented challenge facing the scientific community. Across a wide frequency spectrum and scattering-vector range, scattering-based techniques have been developed and utilized to study the dynamics in disordered systems (Grübel & Zontone, 2004). Prominent examples include Raman spectroscopy (Palmer, 2004), Brillouin scattering (Elmroth *et al.*, 1992), dynamic light scattering (DLS) (van Megen & Pusey, 1991), inelastic X-ray scattering (Sette *et al.*, 1995) and inelastic neutron scattering (Doster *et al.*, 1990).

Another technique that has drawn much attention in recent years is X-ray photon correlation spectroscopy (XPCS), due to the rapid development of light sources across the globe over the last two decades (Grübel & Zontone, 2004; Sutton, 2008; Leheny, 2012). These light sources, which include third-generation synchrotron radiation sources and free-electron laser sources, produce and deliver coherent X-ray beams several orders of magnitude more intense than previously available (Sandy *et al.*, 1999; Abernathy *et al.*, 1998; Tiedtke *et al.*, 2009; Grübel, 2008; Grübel *et al.*, 2007). The access to coherent X-rays opens up opportunities for coherent X-ray scattering (Livet & Sutton, 2012; Leheny, 2012), coherent X-ray diffraction (Miao *et al.*, 1999, 2002) and coherent X-ray imaging (Mayo *et al.*, 2003; Snigirev *et al.*, 1995). XPCS, an extension of coherent X-ray scattering, is fundamentally similar to DLS. It probes the dynamic timescale of equilibrium and near-equilibrium processes by monitoring the intensity fluctuations of coherent speckles and the correlation functions associated with these intensity fluctuations. The speckles originate from the coherent interference of scattered light from a material where spatial inhomogeneities are present (Sutton *et al.*, 1991). Because measurements of correlation functions generally possess scattering-vector dependence, they provide insight into variations in dynamics with length scale that can illuminate the microscopic origins of the underlying physical processes.

Since its development (Brauer *et al.*, 1995; Dierker *et al.*, 1995), XPCS has led to significant progress in our understanding of a wide variety of important dynamic phenomena, and this has impacted many areas of condensed matter physics and material physics. Examples include observation of equi-

librium dynamics in disordered hard materials such as alloys (Brauer *et al.*, 1995) and glasses (Malik *et al.*, 1998; Ruta *et al.*, 2012), and various aspects relevant to soft materials, such as the dynamics of concentrated colloidal suspensions (Lurio *et al.*, 2000; Guo *et al.*, 2010; Sikorski *et al.*, 2011), dynamics near colloidal glass transitions (Pontoni *et al.*, 2003) and dynamics in polymer systems (Mochrie *et al.*, 1997; Falus *et al.*, 2005; Guo *et al.*, 2009), and in jammed systems (Chen *et al.*, 2013). When applied in a grazing-incidence geometry, XPCS has proven to be successful in detecting capillary wave dynamics (Seydel *et al.*, 2001; Jiang *et al.*, 2007).

The majority of the available XPCS studies seek to enhance our understanding of equilibrium dynamics by invoking the first-order intensity correlation function. It is worth noting that the age-dependent nonequilibrium dynamics can also be identified and characterized by using a two-time correlation function in a multiple-speckle time-correlation scheme (Madsen *et al.*, 2010). This method was pioneered by Sutton *et al.* (Malik *et al.*, 1998), and has been successfully applied to probe the slow ageing dynamics in alloys (Malik *et al.*, 1998; Muller *et al.*, 2011), gel formation and ageing in suspensions of silica nanocolloids (Guo *et al.*, 2011), and relaxation of depletion gels following shear (Chung *et al.*, 2006), among others (Guo *et al.*, 2007; Lu *et al.*, 2008). However, in order to reveal the temporal variation of the correlations, a valid time averaging over the experiment is required, which restricts this analysis to slowly evolving and/or near-equilibrium dynamics. At the same time, because conventional synchrotron XPCS utilizes a pinhole geometry scattering configuration, its resolution and accessible reciprocal-vector range are both limited. Notably, there is an effective gap between the accessible reciprocal-vector ranges of DLS and XPCS (Grübel & Zontone, 2004; Zhang, Allen, Levine, Ilavsky & Long, 2012).

We have recently developed an XPCS technique based on crystal optics that exploit a Bonse–Hart geometry (Bonse & Hart, 1965). This technique, referred to as ultra small angle X-ray scattering–X-ray photon correlation spectroscopy (USAXS–XPCS), is capable of probing the slow equilibrium and nonequilibrium dynamics of optically opaque materials with features in a size range from 100 nm to several micrometres (Zhang *et al.*, 2011). In other words, USAXS–XPCS fills the aforementioned gap between the accessible reciprocal-vector ranges of XPCS and DLS. The applicable size range of USAXS–XPCS also makes it relevant to a large class of functional materials whose properties are tightly knitted to their microstructures. Similar to conventional XPCS, USAXS–XPCS has proven useful in studying equilibrium dynamics and revealing the wavevector dependence of relaxation timescales (Zhang, Allen, Levine, Ilavsky & Long, 2013). Owing to the sensitivity provided by the interference of short-wavelength coherent X-rays, USAXS–XPCS in a scan mode can also serve as a structural probe that detects subtle local structural variations prior to changes in the bulk microstructure, as shown in our previous investigations of the onset of amorphous-to-crystalline transformation in amorphous calcium phosphate based composite materials (Zhang, Allen, Levine, Espinal *et al.*, 2012). Moreover, we have used

USAXS–XPCS in its scan mode to probe the timescale associated with nonequilibrium dynamics in materials under various conditions pertinent to material performance (Zhang, Allen, Levine, Vaudin *et al.*, 2013). In spite of these successes, a rigorous connection between measured nonequilibrium dynamic timescales and underlying physical processes remains lacking. A similar statement can also be made about the applications of conventional pinhole-based XPCS in detecting nonequilibrium dynamic processes. Conceptually, understanding nonequilibrium processes and systems will require addressing the major difficulties associated with bridging theories across many length and time scales. New concepts and approaches will be needed.

Simulations bridge theories and experiments together and provide a unique perspective on the underlying principles that govern a given physical process. In the time and length scales that are relevant to USAXS–XPCS, the three-dimensional finite element analysis (FEA) approach provides the proper time- and length-scale resolution that enables a detailed description of complex dynamic behaviors of materials. Additionally, for the length scale that is relevant to USAXS–XPCS (all greater than 100 nm), it is known that the laws of continuum solid mechanics dominate (Guz *et al.*, 2007), which forms the foundation of FEA.

In this article, we will first describe a simple composite system, static and dynamic measurements that we performed on this system, as well as the methods of data interpretation. We will introduce the FEA simulation method that we adopted, including the simulation parameters and the assumptions that we made to simplify and facilitate the simulation. We will then present and discuss the experimental and simulation results, and finish with some concluding remarks.

2. Material system

Commercially available barium boron aluminium silicate glass fillers were obtained from Caulk/Dentsply (Milford, DE, USA; lot No. 07033).[1] The polymer matrix was formulated from commercially available dental monomers and photo-initiators used for visible light polymerization. 2,2-Bis-[(*p*-2′-hydroxy-3′-methacryloxypropoxy)phenyl]-propane (Bis-GMA) and triethyleneglycol dimethacrylate (TEGDMA) were used in a 50:50 mass ratio. Bis-GMA/TEGDMA resin was photo-activated by the inclusion of camphorquinone (mass fraction 0.2%) and ethyl-4,4-*N*,*N*-dimethylamino-benzoate (mass fraction 0.8%).

Composite pastes were formulated by hand-mixing photo-activated Bis-GMA/TEGDMA resin (60% mass fraction) and the glass fillers (40% mass fraction). The pastes were mixed until a uniform consistency was achieved, with no remaining visible filler particulates, and then kept under moderate

---

[1] Certain commercial materials and equipment are identified in this paper only to specify adequately the experimental procedure. In no case does such identification imply recommendation by NIST nor does it imply that the material or equipment identified is necessarily the best available for this purpose.

Li Ma *et al.* · Unveiling the origin of a nonequilibrium dynamic process

vacuum (2.7 kPa) overnight to remove air trapped during mixing. The pastes were molded to form discs (~10 mm diameter, ~1 mm in thickness) by filling the circular openings of flat Teflon molds. The filled molds were covered with Mylar films and glass slides, and then clamped tightly with spring clips. The composite discs were cured by means of a 120 s photo-polymerization (Triad 2000, Dentsply International, York, PA, USA) procedure described elsewhere (Skrtic & Antonucci, 2003). The composites were stored in dry air for at least 24 h.

3. Experiments and methods

In this work, we investigated a transient structural change (a nonequilibrium process) associated with an isothermal anneal in a glass–polymer composite system with both static USAXS and dynamic USAXS–XPCS.

3.1. USAXS measurements

We conducted USAXS measurements using the USAXS instrument at ChemMatCARS sector 15-ID at the Advanced Photon Source (APS), Argonne National Laboratory, IL, USA (Ilavsky *et al.*, 2009, 2013). This instrument employs Bonse–Hart-type double-crystal optics to extend the scattering-vector q range of small-angle X-ray scattering down to 1×10^{-4} Å^{-1} [where $q = 4\pi/\lambda \times \sin(\theta)$, λ is the X-ray wavelength and 2θ is the scattering angle]. We used collimated monochromatic X-rays in a transmission geometry to measure the scattering intensity as a function of q. The X-ray energy was 10.5 keV, corresponding to an X-ray wavelength of 1.18 Å. The instrument was operated in two-dimensional collimated mode with beam-defining slits set at 0.5×0.5 mm. USAXS measurements were performed in the q range from 10^{-4} to 10^{-1} Å^{-1}. The q resolution was approximately 1.5×10^{-4} Å^{-1} and the incident photon flux on the sample was of the order of 1×10^{12} photon s^{-1}. We collected 150 data points which were logarithmically distributed through the q range. Data collection time for each data point was 1 s.

We loaded the sample disc into a Linkam TH600 thermal stage with polyamide entrance and exit windows (Linkam Scientific Instruments Ltd, Tadworth, UK). The temperature control was assisted with liquid-nitrogen circulation for rapid heating and cooling. The heating/cooling rate was set at 50 K min^{-1}. To examine the effect an isothermal treatment had on the statistically significant microstructure of the specimen, we performed USAXS measurements both at room temperature and at 388 K, which is above the glass transition temperature of the polymer resins at approximately 358 K.

3.2. USAXS–XPCS measurements

We conducted the USAXS–XPCS measurements also using the USAXS instrument at the APS. The instrumental configuration for this type of coherent scattering experiment was described previously (Zhang *et al.*, 2011). Compared with the standard USAXS configuration, the most notable difference is that a pair of 15×15 µm coherence-defining slits was placed in front of the collimating crystals as a secondary coherent source. Samples were loaded into the temperature cell as described above. Because the microstructural variation in this composite material upon heating is nonequilibrium in nature, we elected to perform this study with USAXS–XPCS in its scan mode (Zhang, Allen, Levine, Ilavsky & Long, 2012; Zhang *et al.*, 2011).

We followed an established procedure that offers the best time resolution while maintaining the optimal alignment of the instrument (Zhang, Allen, Levine, Ilavsky & Long, 2012; Zhang *et al.*, 2011). For USAXS–XPCS measurements, once the annealing temperature of 388 K was reached, we started a 100-point USAXS–XPCS scan covering a q range from -1.3×10^{-4} to 1×10^{-3} Å^{-1}. For each data point, the data acquisition time was 1 s. This scan included the rocking-curve section of the scattering profile, which defines the forward scattering ($q = 0$) direction. This 100-point scan took approximately 180 s to complete. We denote this as a 'long' scan.

Following each 'long' scan, we took five 'short' scans over the q range 1×10^{-4} to 1×10^{-3} Å^{-1}. Each short scan had 50 data points and took ~90 s to complete, taking into account the time that it took for the USAXS scanning stages to return to their respective starting positions.

A set of USAXS–XPCS scans consists of one 'long' scan and five 'short' scans. After a set, we retuned the optics to verify that the alignment of the instrument remained optimal before starting another set of long and short scans. Retuning of the instrument took ~120 s. The total measurement time was based on the amount of time required for the material system to reach equilibrium, *i.e.* until the scanning profiles no longer showed any significant changes from scan to scan. The total measurement time for the USAXS–XPCS measurement reported in this article was approximately 1 h.

3.3. Finite element modeling

We conducted three-dimensional FEA modeling with the commercial FEA software *Abaqus*. In this simulation, we seek to understand the connection between local structure changes induced by stress relaxation and the experimentally identified relaxation process and its timescale in this concentrated and inherently jammed system.

To obtain accurate solutions, simulations of composite materials require the material properties of each material component to be represented. In our system, the high mass fraction of the glass fillers led to a high filler number density, which inevitably resulted in a large number of nodes in the three-dimensional mesh. To effectively reduce the number of nodes and preserve the underlying physical process, we made some necessary simplifications that will be detailed below.

Our disc sample had a diameter of 10 mm and a thickness of 1 mm. We have previously shown that the coherence of the X-rays from an APS undulator A source allows the entire illuminated sample volume to be probed coherently along the longitudinal direction at the angular regime accessible to USAXS–XPCS (Zhang *et al.*, 2011). Here, due to the large

number of filler particles, without losing statistical significance, we reduced the modeled sample thickness to 500 µm. We performed a parameter study to decide the diameter of the disc used in the simulations. We found that with a 15 × 15 µm X-ray illuminated area at the center, an outer diameter D of 500 µm was sufficiently large to avoid boundary effects. Because coherent X-rays only probe microstructures within the beam path, we disregarded the filler particles outside of the illuminated zone and assumed their effects on the simulation results to be negligible. We also assumed that the filler particles have a uniform diameter of 2 µm. This assumption served two purposes. First, it eliminates the complications that a size distribution of the filler particles introduces to the creation of the mesh. Second, this larger diameter reduces the total number of filler particles at a constant filler volume, which again effectively reduces the number of elements in the three-dimensional mesh.

The geometry of the modeled sample is shown in Fig. 1(a). The center block, which shows the path of coherent X-rays, is illustrated in Fig. 1(b). Here, within a volume of 15 × 15 × 500 µm, we randomly generated positions for 5370 spherical filler particles. The total volume fraction of the filler particles in the center block was approximately 20%, which converts to a 40% mass fraction when taking into account the density of the filler particles. We maintained a minimal distance between any pair of filler particles of 0.05 times the particle diameter, due to practical limitations imposed by the requirements of the finite element discretization. For similar reasons, the

minimal distance between a sphere surface and the boundary of the center block was set to 0.05 µm so that near-boundary distortions of the finite elements were prevented during meshing.

Following these simplifications, we created finite elements in the center block with a custom-made plug-in program for *Abaqus*. Given the sizes and positions of each filler particle, this program automatically meshed each particle with 224 eight-node linear brick elements with coupled temperature and displacement. We meshed the polymer matrix in the center block with 3.05 million four-node linear tetrahedron elements with coupled temperature and displacement. The contacting surfaces of the particle and matrix elements are tied together to prevent interface sliding and delamination. The disc volume external to the center block was also meshed with eight-node linear brick elements with coupled temperature and displacement. During meshing, we took special care to avoid distorted elements, particularly in the regions where local volume fractions of the filler particles were high. Altogether, the total number of elements for the entire model was approximately 4.48 million. The final mesh model and a section of the amplified center block are shown in Figs. 2(a) and 2(b), respectively.

The three-dimensional FEA simulation was performed within the context of finite deformation theory, where true (Cauchy) stresses and logarithmic strains were used in the constitutive equations. It was assumed that the filler particles behave as elastic and isotropic solids. At temperatures above
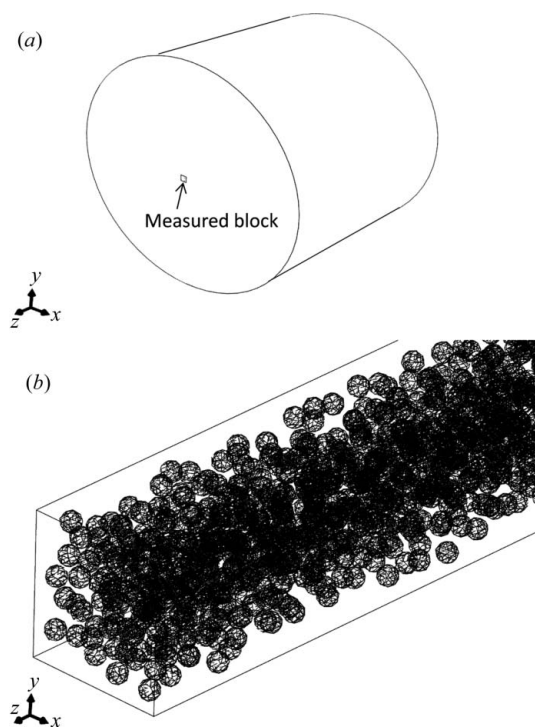

Figure 1
(a) Schematic showing the sample geometry used in three-dimensional FEA modeling. (b) A snapshot of the center (measured) block showing the details related to the spatial distribution and meshing of the filler particles.
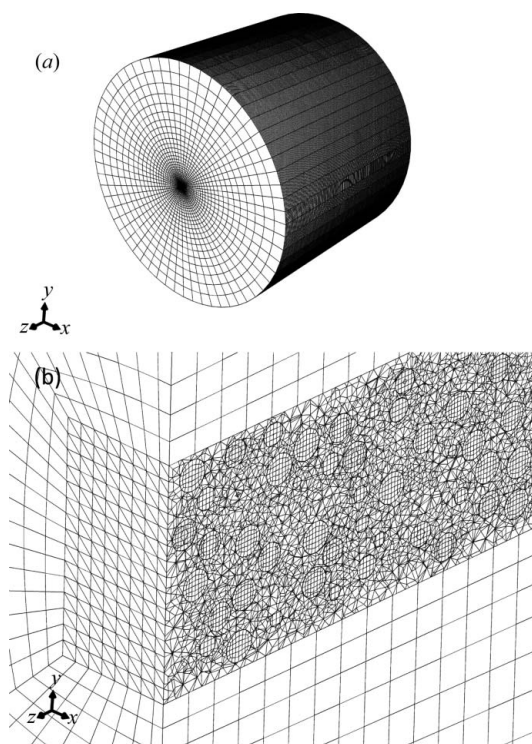

Figure 2
Schematics showing (a) meshing of the entire modeled volume and (b) the details of meshing with a cross section of the amplified center block, where different meshing densities were used for the filler particles and the polymeric materials that surround them.

Table 1
Material properties of SiO₂ and BisGMA.

	Filler particle SiO₂†	Polymer matrix BisGMA (Mark, 1996)
Young's modulus (GPa)	73	1.1 (T = 298 K)
		0.2 (T = 358 K)
Possion's ratio	0.17	0.35
Yield stress (GPa)	8	
Density (kg m⁻³)	2329	1.181 (T = 313 K)
		1.177 (T = 333 K)
		1.171 (T = 353 K)
		1.166 (T = 373 K)
		1.162 (T = 393 K)
Thermal expansion [K⁻¹]	5.50×10^{-7}	1.8×10^{-4} (T = 313 K)
		2.1×10^{-4} (T = 333 K)
		2.4×10^{-4} (T = 353 K)
		2.7×10^{-4} (T = 373 K)
		5.5×10^{-4} (T = 393 K)
Specific heat [J(kg K)⁻¹]	713 (T = 298 K)	1765 (T = 298 K)
	785 (T = 398 K)	2143 (T = 500 K)
Thermal conductivity [W(m K)⁻¹]	124	0.21
Latent heat (J g⁻¹)		173.8 (T = 358 K)

† http://www.sciner.com/Opticsland/FS.htm

Table 2
BisGMA viscoelastic parameters.

i	$\overline{g}_i^P$	τ_i (s)
1	0.3175	0.087
2	0.1845	86.8
3	0.1272	1948
4	0.0179	25809

glass transition temperature, the material behavior of the polymer matrix was viscoelastic. The material properties of the filler particles and the polymer matrix are listed in Table 1.

To resemble the experimental process, we conducted the simulation in two steps. The starting configuration was the FEA particle/matrix system described above. The system was stress free at room temperature (298 K). First, we instantaneously increased the temperature to 378 K, using a fully coupled temperature displacement procedure and solving for the stress/displacement field and the temperature field simultaneously. We integrated the heat transfer equations with a backward-difference scheme and adopted Newton's method as the numerical solver. In the second step, we conducted a quasi-static stress analysis to calculate the motions of the filler particles in response to the viscoelastic relaxations of the polymer matrix during a simulated 30 min time frame. The local stresses, strains and particle positions were saved every 6 s of simulated time except during the early stage of relaxation when changes occurred more rapidly. We described the time domain viscoelasticity of the polymer matrix with a Prony series expansion of the dimensionless relaxation modulus g_r:

$$g_R(t) = 1 - \sum_{i=1}^{N} \overline{g}_i^P [1 - \exp(-t/\tau_i)], \qquad (1)$$

where N, $\overline{g}_i^P$, τ_i and i = 1, 2, ..., N are Prony constants specific to the materials. These Prony constants were derived using least-squares fitting of available experimental data (Singh *et al.*, 2010). These constants are shown in Table 2. The simulation used 120 CPUs and 80 GB minimum memory. Completion of this simulation required over 86 000 CPU hours.

4. Results and discussion

The USAXS data were corrected with the background scattering profile of the sample chamber acquired under identical experimental conditions and the analysis was conducted with the Irena SAS analysis package (Ilavsky & Jemian, 2009). To reduce the size distribution of the particles, we applied a maximum entropy (MaxEnt) size distribution analysis method, which does not make *a priori* assumptions about the shape of the particle size distribution. It was assumed that these glass filler particles are spherical in shape, as suggested by previous scanning electron microscopy work (Zhang, Allen, Levine, Espinal *et al.*, 2012). To assess the uncertainty of the results, we varied the scattering data by introducing a random Gaussian noise, which was scaled to the original uncertainty of the scattering intensity, and performed this MaxEnt analysis ten times with different sets of random noise. We statistically analyzed the ten sets of results. USAXS data and size distribution of the filler particles are shown in Fig. 3. Based on the statistics of the results, we found that the diameters of the filler particles follow a broad size distribution centered at 4000 Å. More significantly, Fig. 3 shows the USAXS profiles acquired before heating and after heating overlap with each other. This result has two possible implications: heating of the glass composites does not induce structural change in the samples, or USAXS, as a statistically representative technique, is inadequate for detecting the resulting local changes in microstructure.
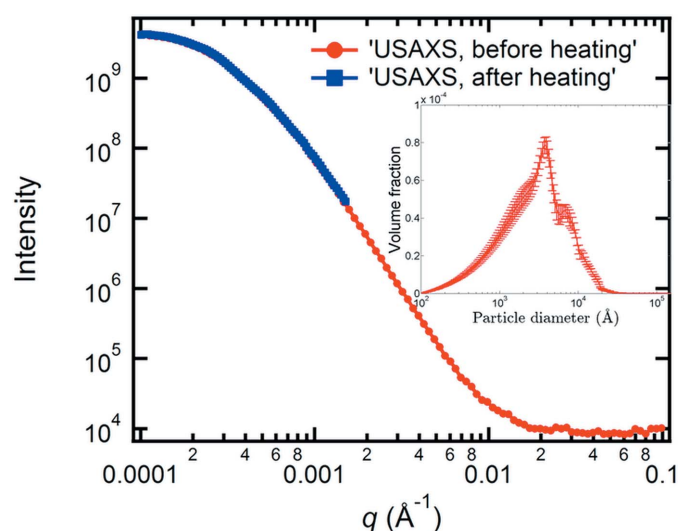

Figure 3
USAXS profile of glass composite. The inset shows the volume size distribution of the glass filler particles. The uncertainty on the volume size distribution was drawn from ten MaxEnt analyses of the USAXS data.

USAXS–XPCS was used to distinguish between these two possibilities. Intensities yielded by USAXS–XPCS rely on the coherent interference of X-rays. Within the coherent wavefront, a change in local microstructure leads to phase change, which in turn results in a change in the coherent scattering intensity. Thus, USAXS–XPCS in a scan mode, in principle, should be able to capture local changes in microstructure, should these occur (the changing speckle patterns described above).

Fig. 4(a) shows the USAXS–XPCS patterns of the glass composite acquired at 0, 20 and 40 min after the start of heating. Compared with Fig. 3, which shows a smooth curve over its q range, 'speckles' characteristic of coherent scattering

appear in the USAXS–XPCS patterns. With fully coherent illumination, the linear dimension of the speckle on a two-dimensional detector (speckle size) is $s = \lambda \times z_{sd}/d$, where λ is the wavelength of radiation, z_{sd} is the sample-to-detector distance and d is the size of the beam (Goodman, 1975; Paterson *et al.*, 2001). With the USAXS–XPCS experimental parameters, we find an estimated speckle size in reciprocal space of $0.4 \times 10^{-4}\,\text{Å}^{-1}$, which is very similar to the full width at half-maximum of the speckles shown in Fig. 4(a). This result demonstrates the speckle nature of the USAXS–XPCS patterns. These coherent scattering profiles reflect the detailed arrangement of the scattering-length (electron) density in the sampled volume at a given time (Livet, 2007; Nugent, 2010), and no longer overlap. The time-dependent evolution of the USAXS–XPCS patterns reflects the changes in the microstructure and can be used to investigate the dynamic timescales related to the underlying physical process. Additionally, a comparison between Fig. 4(a) and Fig. 3 provides direct evidence in proving that bulk, incoherent-scattering-based measurement techniques such as USAXS may not provide the sensitivity required to detect subtle local structural rearrangements.

To extract the timescale related to this nonequilibrium process, we followed a previously established data reduction and analysis procedure that was reported elsewhere (Zhang *et al.*, 2011). In this procedure, the reduction of the USAXS–XPCS data centers on normalizations by both the scattering-invariant and the incoherently summed USAXS intensity, which place the often-logarithmic small-angle scattering intensity on an approximately linear scale. The analysis relies on the correlation coefficient, $\varphi(i, j)$, a statistical parameter that describes the degree of resemblance between two data sets. We used this correlation coefficient to investigate the correlation behavior in all sets of the reduced USAXS–XPCS data. Here, $\varphi(i, j)$ is defined as $\varphi(i, j) = C(i, j)/[C(i, i) \times C(j, j)]^{1/2}$, where i, j represent the ith and jth data set, and $C(i, j)$ is the covariance of variables i and j, and follows the standard statistical definition $C(i, j) = \langle (i - \langle i \rangle) \times (j - \langle j \rangle) \rangle$, where $\langle \rangle$ represents the statistical mean.

We used a correlation coefficient map to illustrate the changes in the correlation coefficients. Fig. 4(b) shows such a map based on the calculated $\varphi(i, j)$ for our experimental USAXS–XPCS data. In Fig. 4(b), the x and y axes of the figure reflect the start acquisition time of the ith and jth USAXS–XPCS scans, respectively. The color scale shows the magnitude of the correlation coefficient $\varphi(i, j)$. The higher the value is, the more correlated the ith and jth scans are. Fig. 4(b) shows the local structural variation underwent a complicated process. Initially, the microstructure was relatively stable, which was followed by a short period of sharp change at approximately 8 min after reaching the target temperature. The changes that occurred afterwards were more gradual. In particular, Fig. 4(b) shows that approximately 40 min after reaching the target temperature, the system reached a stable state signified by the red triangle to the right of the dashed line. Following this protocol, we were able to extract the timescales for the
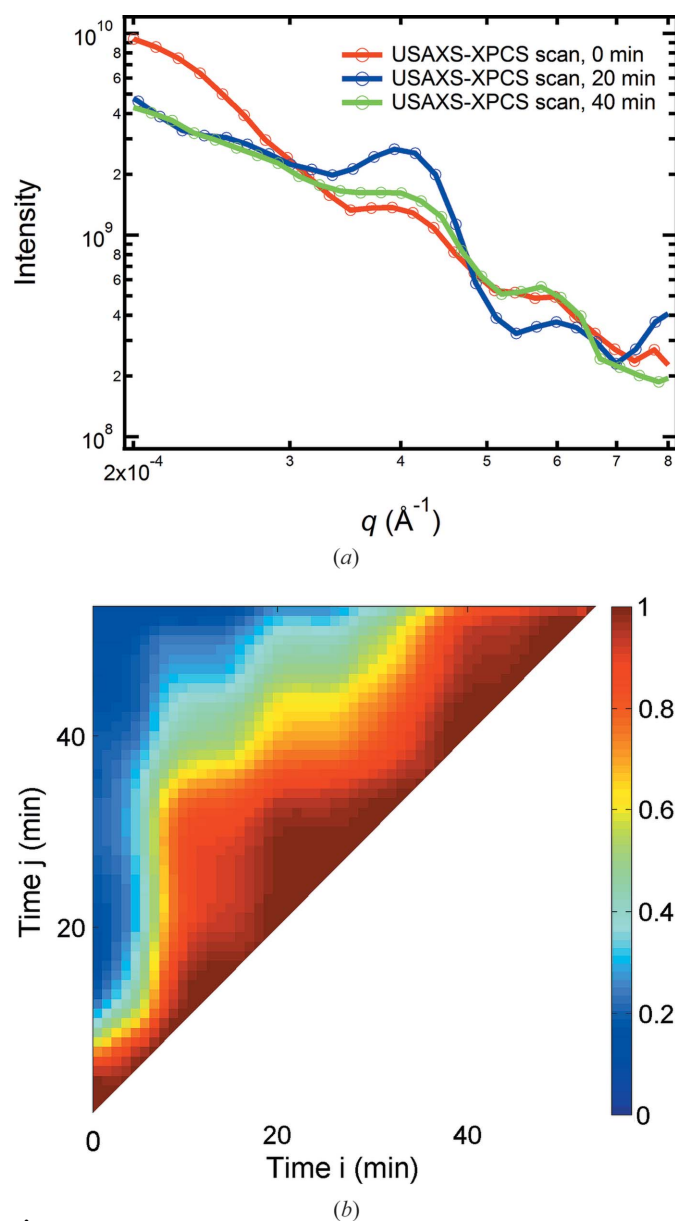
Figure 4
(a) A comparison of USAXS–XPCS speckle patterns acquired at different times (0, 20, 40 min) after the target temperature was reached. The standard deviation uncertainties are smaller than the symbols for the data points. (b) Calculated correlation coefficient maps based on the experimentally acquired USAXS–XPCS scan patterns.

nonequilibrium processes of these composite materials under a variety of physical and chemical conditions, such as different heating temperatures and acidic strengths (Zhang, Allen, Levine, Espinal *et al.*, 2012; Zhang, Allen, Levine, Vaudin *et al.*, 2013). Despite this, up to now, we have not had the tools to account for the effects that the underlying processes have on the correlation coefficient map *prior to* the arrival of a final stable state.

For this purpose, we performed the aforementioned three-dimensional FEA modeling to investigate the nonequilibrium relaxation of the modeled composite material at elevated temperature. The initial state of the composite material was completely relaxed. During the first step of the simulation, we assumed that the heating from room temperature to 388 K was instantaneous. We adopted a steady-state simulation approach at this point. The mismatch between the thermal expansion coefficients of the filler particles and the polymer matrix resulted in a distribution of local stress. This distribution is illustrated in Fig. 5(*a*). Here, we only plotted the principal stress on the surface of the filler particles. It is evident that the principal stress field is highly nonuniform and extremely localized. As expected, a lower local particle density in general led to a lower local stress. The stress ranges between 36 and 1239 MPa with the majority of the stresses less than 270 MPa. The stress distribution in Fig. 5(*a*) served as the initial state for the second part of this simulation, which describes a transient and isothermal process. Here, with the temperature above the glass transition temperature of the polymer matrix, the matrix displays a highly viscous behavior, which would allow the spatial redistribution of the filler particles due to the relaxation of the nonuniform stress field. Figs. 5(*b*) and 5(*c*) show the principal stress on the same section of the modeled material as in Fig. 5(*a*) at 4.2 and 30 min after relaxation started. The nonuniformity in the stress field clearly dissipated as the
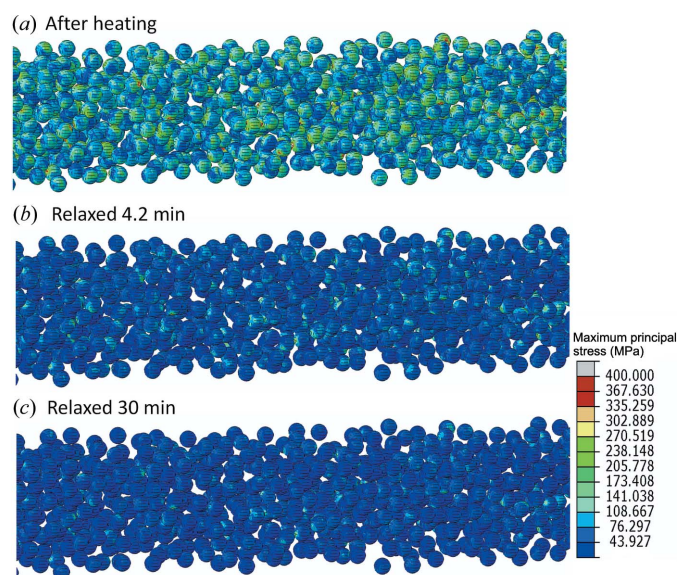
relaxation process progressed. Similarly, we found that at 4.2 min, the stress ranges between 15 and 667 MPa with the majority of stresses less than 140 MPa, and at 30 min the stress ranges between 12 and 518 MPa with the majority of stresses less than 76 MPa.

Fig. 6 shows the evolution of the equivalent creep strain, which is defined as the difference between the total strain and the elastic strain, of the polymer matrix of the same cross section. The equivalent creep strain highlights the sample volumes that experience the largest structural changes. Although the local strain appears to have a complex dependence on the local morphology, a close examination of Fig. 6 suggests that a higher local density of the filler particles yielded a higher strain in the polymer matrix, *i.e.* a larger displacement of the filler particles. This is in accordance with a higher initial stress at such locations resulting from the initial heating process. We also highlighted a few locations in Fig. 6 that illustrate particle movements as a function of time during the relaxation process.

To compare the simulation results with our experimental findings, we calculated the time-dependent coherent scattering intensity based on the spatial distribution of the electron density inside the composite material as calculated by the FEA modeling. We adopted a first-principle-based wave-optics approach to perform this calculation. This approach is similar to the phase propagation method widely adopted in simulations of coherent X-ray imaging and scattering (Paganin, 2006; Zhang *et al.*, 2008).

In a coherent scattering event, phase change occurs when an incident wave illuminates a scattering object. In the far field, at small-angle limits, the observed intensity is a result of the coherent interference of these scattered spherical waves. Because the scattering cross section of X-rays is low, the complex amplitude at the exit interface of the sample can be approximated as the transmitted wave. To calculate this transmitted wavefront, we define the complex refractive index in the X-ray regime as $n = 1 - \delta + i\beta$, where δ is the refraction decrement and β is the imaginary attenuation decrement.

Figure 5
Contour plot of the maximum principal stresses in particles (*a*) after heating, (*b*) 4.2 min after the start of relaxation and (*c*) 30 min after the start of relaxation.
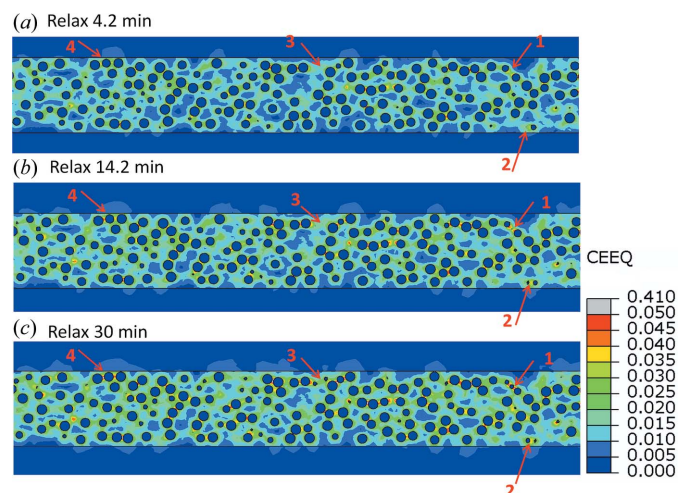

Figure 6
Contour of TEGDMA equivalent creep strain in two dimensions (*a*) 4.2 min, (*b*) 14.2 min and (*c*) 30 min after the start of relaxation.

Table 3
Calculated refractive indices for SiO₂ and BisGMA.

	Refractive decrement δ	Absorption decrement β
SiO$_2$	4.60×10^{-6}	3.89×10^{-8}
BisGMA	2.67×10^{-6}	0.29×10^{-8}

With an incident plane wave, the transmitted complex field immediately after the sample $E(x_0, y_0)$ can be written as:

$$E(x_0, y_0) = E_0 \exp(-ikz_0) \times \exp[i\varphi(x_0, y_0) - \mu(x_0, y_0)], \quad (2)$$

where

$$\varphi(x_0, y_0) = 2\pi/\lambda \int \delta(x_0, y_0, z)\, \mathrm{d}z \quad (3)$$

and

$$\mu(x_0, y_0) = 2\pi/\lambda \int \beta(x_0, y_0, z)\, \mathrm{d}z. \quad (4)$$

Here, x_0 and y_0 specify the spatial coordinates, E_0 is the amplitude of the incident coherent X-ray wave, $k = 2\pi/\lambda$ is the magnitude of the wavevector, λ is the X-ray wavelength, z_0 is the sample thickness, and $\varphi(x_0, y_0)$ and $\mu(x_0, y_0)$ are the real and imaginary components of the phase shift, respectively. Following a standard Huygens–Fresnel treatment (Zhang *et al.*, 2008), we obtain the reciprocal-space coherent scattering intensity at the detector in the far field as

$$I(q_x, q_y) = A^2 \left| \int_{-\infty}^{\infty} E(x_0, y_0) \times \exp\left[-i\frac{2\pi}{\lambda z}(q_x x + q_y y)\right] \mathrm{d}x\, \mathrm{d}y \right|^2 \quad (5)$$

where q_x and q_y are the spatial components of the reciprocal vector q, z is the sample-to-detector distance and A is a multiplicative factor. Equation (5) explicitly shows that the coherent scattering intensity at the detector is proportional to the Fourier transform of the transmitted wave at the exit interface of the sample, and is the basis to connect the simulation and experimental results. We also point out that equation (5) also gives rise to a highly nonuniform pattern on a two-dimensional detector, *i.e.* a speckle pattern. Based on this calculated speckle pattern, USAXS–XPCS profiles are readily obtained along the vertical scan direction of the USAXS instrument.

In this calculation, to simplify the simulation without losing generality, we assumed that the X-ray wave impinging on the sample is spatially and temporally fully coherent, with an X-ray energy of 10.5 keV. We set the detector as a 1024 × 1024 pixel array with a pixel size equal to 50 × 50 µm to match the resolution of the crystal optics used in the experiments. We adopted an aliasing filter to ensure that the Fourier transform is alias free (Zhang *et al.*, 2008). We also used a square aperture to smear the calculated coherent scattering intensity to account for the finite widths of the analyzer crystal rocking curves along both the vertical and horizontal directions. We calculated the refraction and absorption increments of both the filler particles and the matrix as listed in Table 3. With the known size of the filler particles and the simulation-derived particle coordinates, we calculated the time-dependent
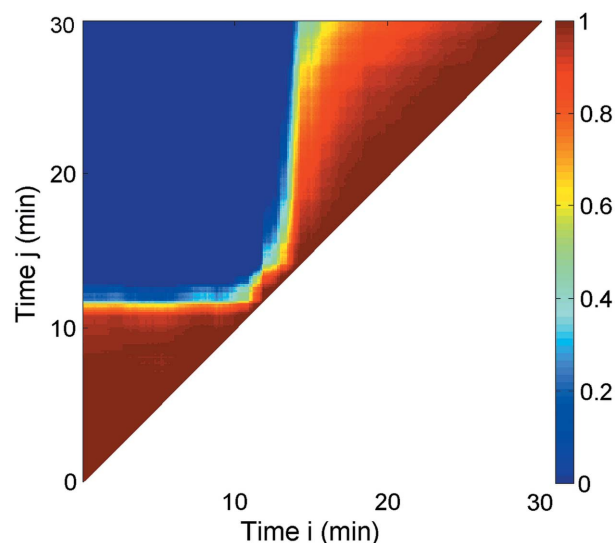

Figure 7
Calculated correlation coefficient map based on the time-dependent filler particle coordinates provided by FEA modeling.

intensity distribution on the detector following equations (2) to (5) with an approximate qr scaling taken into consideration. qr scaling, which scales the relevant q range (q) in the reciprocal space according to the size of interest (r), is necessary because of the discrepancy between the size of the filler particles used in our FEA model and found in our experiment. We then calculated the correlation coefficient map based on these time-dependent, calculated USAXS–XPCS intensity profiles following the identical procedure as in our analysis of the experimental data. This correlation coefficient map is shown in Fig. 7. Despite the simplifications that we made to facilitate the FEA modeling, we found remarkable agreements with the experimental findings (Fig. 4*b*). As with the experimental findings, we identified a relatively stable period in the local microstructures during the initial phase of the simulation. The sharp change occurred at approximately 12 min of time, instead of 8 min in the experiments. The simulation also suggested that after this period of sharp change, the filler rearrangement was more gradual. We also identified that the time that it took for the modeled composite system to reach a stable state is about half of the time found in the experiments. Given the differences between the actual experimental conditions and those imposed by the need for simplifying assumptions in the simulation, the agreement between experiment and simulation was considered acceptable. Indeed, the agreement is sufficient to strongly suggest that the relaxation of the nonuniform stress field introduced by rapid heating is the cause of the observed dynamical process, thus providing additional insights for the underlying process that have been missing in our previous experimental investigations of XPCS-based nonequilibrium dynamics.

5. Concluding remarks

We have performed an experimental study of the static and dynamic structure of a glass filler particle based polymer

research papers

composite at a temperature higher than the glass transition temperature of the polymer matrix with USAXS and USAXS–XPCS, respectively. We found that the static structures, as revealed by USAXS, show no signs of change through an isothermal heating process. USAXS–XPCS, on the other hand, unambiguously shows the changes in the dynamic structure as a function of time. We further conducted a correlation coefficient analysis of the time-dependent USAXS–XPCS profiles, and revealed the dynamic timescale associated with this process.

To better understand the underlying process, we successfully developed a multi-physics finite element model for solving the complex microstructure rearrangement of a slightly simplified composite system. By performing a quasi-static FEA simulation at an elevated temperature, we found that the nonequilibrium dynamics observed in our measurements were caused by the relaxation of a nonuniform stress field associated with thermal mismatch during the initial heating process. Although the underlying physics is not overwhelmingly sophisticated, the many-body nature of this particular composite system makes a detailed account of the transient rearrangement of the filler particles impossible through a conventional theoretical route. FEA simulation provided an appropriate means to describe the underlying process.

We linked the simulation results with the experimental findings using a calculation based on wave propagation theory. We found that, despite the simplifications made to the simulation, a similar timescale to that for the experimental results was identified. Additionally, we found that the correlation coefficient maps from simulation and experiment bear a remarkable resemblance that we speculate is characteristic of this type of structural rearrangement.

It is a well known challenge to characterize nonequilibrium processes. Various XPCS techniques can potentially contribute to an improved understanding of these complex processes. This work presents, to the best of our knowledge, the first attempt to directly connect the nonequilibrium dynamics observed in XPCS measurements and the detailed underlying processes through a simulation approach. While our model system is notably simple, we believe that with careful modification, the method introduced in our work can be readily extended to other more complicated and technically more important real materials. This will inevitably lead to materials with better characteristics and behaviors.

References

Abernathy, D. L., Grübel, G., Brauer, S., McNulty, I., Stephenson, G. B., Mochrie, S. G. J., Sandy, A. R., Mulders, N. & Sutton, M. (1998). *J. Synchrotron Rad.* **5**, 37–47.

Bonse, U. & Hart, M. (1965). *Appl. Phys. Lett.* **7**, 238–240.

Brauer, S., Stephenson, G. B., Sutton, M., Brüning, R., Dufresne, E., Mochrie, S. G., Grübel, G., Als-Nielsen, J. & Abernathy, D. L. (1995). *Phys. Rev. Lett.* **74**, 2010–2013.

Chen, S. W., Guo, H., Seu, K. A., Dumesnil, K., Roy, S. & Sinha, S. K. (2013). *Phys. Rev. Lett.* **110**, 217201.

Chung, B., Ramakrishnan, S., Bandyopadhyay, R., Liang, D., Zukoski, C. F., Harden, J. L. & Leheny, R. L. (2006). *Phys. Rev. Lett.* **96**, 228301.

Dierker, S. B., Pindak, R., Fleming, R. M., Robinson, I. K. & Berman, L. (1995). *Phys. Rev. Lett.* **75**, 449–452.

Doster, W., Cusack, S. & Petry, W. (1990). *Phys. Rev. Lett.* **65**, 1080–1083.

Elmroth, M., Börjesson, L. & Torell, L. M. (1992). *Phys. Rev. Lett.* **68**, 79–82.

Falus, P., Borthwick, M. A. & Mochrie, S. G. (2005). *Phys. Rev. Lett.* **94**, 016105.

Goodman, J. W. (1975). *Laser Speckle and Related Phenomena*, pp. 9–75. Berlin, Heidelberg: Springer.

Grübel, G. (2008). *C. R. Phys.* **9**, 668–680.

Grübel, G., Stephenson, G., Gutt, C., Sinn, H. & Tschentscher, T. (2007). *Nucl. Instrum. Methods Phys. Res. Sect. B*, **262**, 357–367.

Grübel, G. & Zontone, F. (2004). *J. Alloys Compd.* **362**, 3–11.

Guo, H., Bourret, G., Corbierre, M. K., Rucareanu, S., Lennox, R. B., Laaziri, K., Piche, L., Sutton, M., Harden, J. L. & Leheny, R. L. (2009). *Phys. Rev. Lett.* **102**, 075702.

Guo, H., Ramakrishnan, S., Harden, J. L. & Leheny, R. L. (2010). *Phys. Rev. E*, **81**, 050401.

Guo, H. Y., Ramakrishnan, S., Harden, J. L. & Leheny, R. L. (2011). *J. Chem. Phys.* **135**, 154903.

Guo, H., Wilking, J. N., Liang, D., Mason, T. G., Harden, J. L. & Leheny, R. L. (2007). *Phys. Rev. E*, **75**, 041401.

Guz, A. N., Rushchitsky, J. J. & Guz, I. A. (2007). *Int. Appl. Mech.* **43**, 247–271.

Ilavsky, J. & Jemian, P. R. (2009). *J. Appl. Cryst.* **42**, 347–353.

Ilavsky, J., Jemian, P. R., Allen, A. J., Zhang, F., Levine, L. E. & Long, G. G. (2009). *J. Appl. Cryst.* **42**, 469–479.

Ilavsky, J., Zhang, F., Allen, A. J., Levine, L. E., Jemian, P. R. & Long, G. G. (2013). *Metall. Mater. Trans. A*, **44**, 68–76.

Jiang, Z., Kim, H., Jiao, X., Lee, H., Lee, Y. J., Byun, Y., Song, S., Eom, D., Li, C., Rafailovich, M. H., Lurio, L. B. & Sinha, S. K. (2007). *Phys. Rev. Lett.* **98**, 227801.

Leheny, R. L. (2012). *Curr. Opin. Colloid Interface Sci.* **17**, 3–12.

Livet, F. (2007). *Acta Cryst.* A**63**, 87–107.

Livet, F. & Sutton, M. (2012). *C. R. Phys.* **13**, 227–236.

Lu, X., Mochrie, S. G., Narayanan, S., Sandy, A. R. & Sprung, M. (2008). *Phys. Rev. Lett.* **100**, 045701.

Lurio, L. B., Lumma, D., Sandy, A. R., Borthwick, M. A., Falus, P., Mochrie, S. G., Pelletier, J. F., Sutton, M., Regan, L., Malik, A. & Stephenson, G. B. (2000). *Phys. Rev. Lett.* **84**, 785–788.

Madsen, A., Leheny, R. L., Guo, H., Sprung, M. & Czakkel, O. (2010). *New J. Phys.* **12**, 055001.

Malik, A., Sandy, A., Lurio, L., Stephenson, G., Mochrie, S., McNulty, I. & Sutton, M. (1998). *Phys. Rev. Lett.* **81**, 5832–5835.

Mark, J. E. (1996). *Physical Properties of Polymers Handbook*. New York: AIP Press.

Mayo, S., Davis, T., Gureyev, T., Miller, P., Paganin, D., Pogany, A., Stevenson, A. & Wilkins, S. (2003). *Opt. Express*, **11**, 2289–2302.

Megen, W. van & Pusey, P. N. (1991). *Phys. Rev. A*, **43**, 5429–5441.

Miao, J., Charalambous, P., Kirz, J. & Sayre, D. (1999). *Nature (London)*, **400**, 342–344.

Miao, J., Ishikawa, T., Johnson, B., Anderson, E. H., Lai, B. & Hodgson, K. O. (2002). *Phys. Rev. Lett.* **89**, 088303.

Mochrie, S., Mayes, A., Sandy, A., Sutton, M., Brauer, S., Stephenson, G., Abernathy, D. & Grübel, G. (1997). *Phys. Rev. Lett.* **78**, 1275–1278.

Muller, L., Waldorf, M., Gutt, C., Grubel, G., Madsen, A., Finlayson, T. R. & Klemradt, U. (2011). *Phys. Rev. Lett.* **107**, 105701.

Nugent, K. A. (2010). *Adv. Phys.* **59**, 1–99.

Paganin, D. M. (2006). *Coherent X-ray Optics.* Oxford University Press.

Palmer, A. G. (2004). *Chem. Rev.* **104**, 3623–3640.

Paterson, D., Allman, B., McMahon, P., Lin, J., Moldovan, N., Nugent, K., McNulty, I., Chantler, C., Retsch, C., Irving, T. & Mancini, D. (2001). *Opt. Commun.* **195**, 79–84.

Pontoni, D., Narayanan, T., Petit, J. M., Grübel, G. & Beysens, D. (2003). *Phys. Rev. Lett.* **90**, 188301.

Ruta, B., Chushkin, Y., Monaco, G., Cipelletti, L., Pineda, E., Bruna, P., Giordano, V. M. & Gonzalez-Silveira, M. (2012). *Phys. Rev. Lett.* **109**, 165701.

Sandy, A. R., Lurio, L. B., Mochrie, S. G. J., Malik, A., Stephenson, G. B., Pelletier, J. F. & Sutton, M. (1999). *J. Synchrotron Rad.* **6**, 1174–1184.

Sette, F., Ruocco, G., Krisch, M., Bergmann, U., Masciovecchio, C., Mazzacurati, V., Signorelli, G. & Verbeni, R. (1995). *Phys. Rev. Lett.* **75**, 850–853.

Seydel, T., Madsen, A., Tolan, M., Grübel, G. & Press, W. (2001). *Phys. Rev. B*, **63**, 073409.

Sikorski, M., Sandy, A. R. & Narayanan, S. (2011). *Phys. Rev. Lett.* **106**, 188301.

Singh, V., Misra, A., Marangos, O., Park, J., Ye, Q., Kieweg, S. L. & Spencer, P. (2010). *J. Biomed. Mater. Res. B Appl. Biomater.* **95**, 283–290.

Skrtic, D. & Antonucci, J. M. (2003). *Biomaterials*, **24**, 2881–2888.

Snigirev, A., Snigireva, I., Kohn, V., Kuznetsov, S. & Schelokov, I. (1995). *Rev. Sci. Instrum.* **66**, 5486–5492.

Sutton, M. (2008). *C. R. Phys.* **9**, 657–667.

Sutton, M., Mochrie, S. G. J., Greytak, T., Nagler, S. E., Berman, L. E., Held, G. A. & Stephenson, G. B. (1991). *Nature (London)*, **352**, 608–610.

Tiedtke, K. *et al.* (2009). *New J. Phys.* **11**, 023029.

Zhang, F., Allen, A. J., Levine, L. E., Espinal, L., Antonucci, J. M., Skrtic, D., O'Donnell, J. N. R. & Ilavsky, J. (2012). *J. Biomed. Mater. Res. A*, **100**, 1293–1306.

Zhang, F., Allen, A. J., Levine, L. E., Ilavsky, J. & Long, G. G. (2012). *Metall. Mater. Trans. A*, **43**, 1445–1453.

Zhang, F., Allen, A. J., Levine, L. E., Ilavsky, J. & Long, G. G. (2013). *Langmuir*, **29**, 1379–1387.

Zhang, F., Allen, A. J., Levine, L. E., Ilavsky, J., Long, G. G. & Sandy, A. R. (2011). *J. Appl. Cryst.* **44**, 200–212.

Zhang, F., Allen, A. J., Levine, L. E., Vaudin, M. D., Skrtic, D., Antonucci, J. M., Hoffman, K., Giuseppetti, A. A. & Ilavsky, J. (2013). Submitted.

Zhang, F., Long, G. G., Levine, L. E., Ilavsky, J. & Jemian, P. R. (2008). *J. Appl. Cryst.* **41**, 416–427.